



Research Paper

Well-designed 3D ZnIn₂S₄ nanosheets/TiO₂ nanobelts as direct Z-scheme photocatalysts for CO₂ photoreduction into renewable hydrocarbon fuel with high efficiency



Guang Yang^a, Daimei Chen^{a,*}, Hao Ding^{a,*}, Jiejie Feng^a, Jin Z. Zhang^{b,*}, Yongfa Zhu^{c,*}, Saher Hamid^d, Detlef W. Bahnemann^d

^a Beijing Key Laboratory of Materials Utilization of Nonmetallic Minerals and Solid Wastes, National Laboratory of Mineral Materials, School of Materials Science and Technology, China University of Geosciences, Xueyuan Road, Haidian District, Beijing 100083, PR China

^b Department of Chemistry & Biochemistry, University of California, 1156 High Street, Santa Cruz, CA 95064, USA

^c Department of Chemistry, Tsinghua University, Beijing 100084, China

^d Photocatalysis and Nanotechnology Research Unit, Institut fuer Technische Chemie, Leibniz Universitaet Hannover, Callinstrasse 3, D-30167 Hannover, Germany

ARTICLE INFO

Article history:

Received 5 June 2017

Received in revised form 11 July 2017

Accepted 2 August 2017

Available online 5 August 2017

Keywords:

TiO₂

ZnIn₂S₄

Z-Scheme system

Three-dimensional structure

ABSTRACT

A 3-dimensional (3D) ZnIn₂S₄/TiO₂ Z-scheme system has been designed and constructed for photocatalytic reduction of CO₂ into renewable hydrocarbon fuels without the use of a solid-state electron mediator. The unique 3D morphology, achieved by assembling 2D ZnIn₂S₄ nanosheets onto 1D TiO₂ nanobelts, not only provides large surface area but also improves the separation and transfer efficiency of photogenerated electrons and holes. The 3D ZnIn₂S₄/TiO₂ Z-scheme photocatalysts show excellent light-harvesting properties demonstrated in photocatalytic reduction of CO₂, resulting in generation of desired hydrocarbons. The CH₄ production rate of the 3D ZnIn₂S₄/TiO₂ can reach up to 1.135 μmol g⁻¹ h⁻¹, which is about 39-times higher than that of bare ZnIn₂S₄ (0.029 μmol g⁻¹ h⁻¹). The enhanced photocatalytic activity is attributed to effective separation of the charge carriers between ZnIn₂S₄ and TiO₂ through the direct Z-scheme instead of a type-II heterojunction. The photogenerated electrons in TiO₂ nanobelts recombine with the holes in ZnIn₂S₄ nanosheets, and the unrecombined electrons/holes on different active sites have stronger reduction/oxidation abilities, leading to higher photocatalytic activity for CO₂ reduction.

© 2017 Published by Elsevier B.V.

1. Introduction

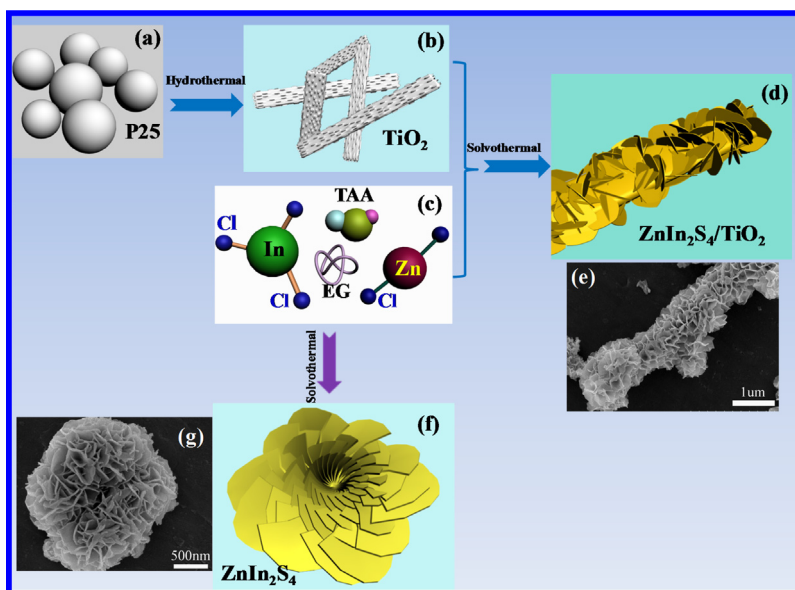
Photocatalytic conversion of carbon dioxide (CO₂) into renewable fuel using solar energy has received increasing attention because this strategy can both reduce the greenhouse gas concentration and relieve the deficiency of energy [1–6]. Although some metal oxides (e.g. TiO₂ and WO₃) and non-oxides (e.g., CdS and Ta₃N₅) have been widely used as photocatalysts, their performance in photocatalytic reactions is still very low [2,6]. Construction of heterostructure photocatalysts (usually type-II heterojunctions) is a common and effective way to broaden the light absorption region and improve the separation efficiency of photoinduced electron-hole pairs, which ultimately results in improved photocatalytic activity [7]. However, in the general type-II heterojunction systems,

redox ability of photoexcited electrons and holes for each reaction is often weakened by the fact that the photogenerated electrons in the conduction band (CB) of one semiconductor would transfer to the CB of another semiconductor with relatively lower band-edge position, while the accumulated holes would transfer to the valence band (VB) of the semiconductor with a higher band-edge position due to the match of bandgap energy levels between these two semiconductors [8,9].

Recently, Z-scheme systems have been developed for water splitting and CO₂ photoreduction [10–12]. Compared with type-II heterostructured photocatalysts, the principal advantage of the Z-scheme systems is not only improved separation efficiency of the photogenerated electron-hole pairs, but also the ability to keep electrons/holes with stronger reduction/oxidation potentials on different active sites [8,13–15]. The photogenerated electrons in the higher conduction band (CB) of one photocatalyst could be used for reduction evolution. Simultaneously, the photogenerated holes in the lower valence band (VB) of the other photocatalyst could be used for oxidation reaction. The primary Z-scheme photocatalysis

* Corresponding authors.

E-mail addresses: chendaimai@cugb.edu.cn (D. Chen), dinghao113@126.com (H. Ding), zhang@ucsc.edu (J.Z. Zhang), zhuyf@tsinghua.edu.cn (Y. Zhu).



Scheme 1. Schematic illustration of the fabrication of 3D ZnIn_2S_4 nanosheets/ TiO_2 nanobelts direct Z-Scheme photocatalysts.

system is comprised of two different semiconductor photocatalysts and a mediator for charge transport. Reversible mediator (e.g., $\text{Fe}^{3+}/\text{Fe}^{2+}$ and IO_3^-/I^-) are usually applied to electron transport chain in Z-scheme photocatalytic systems [16,17]. However, backward reactions, light absorption by the redox mediators and low stability sharply decrease the reactivity of the reversible redox mediator in Z-scheme photocatalytic system [18].

To overcome the above shortcomings, solid-phase Z-scheme systems with appropriate mediators have been developed [8,19]. Reduced graphene oxide (RGO) or mediators (such as noble metals Au and Ag) have often been used as electron mediators [20,21]. The electron mediators provide a pathway through which the photogenerated electrons in one semiconductor can travel and recombine with the holes in another semiconductor quickly, leaving more reductive electrons and more oxidative holes to participate in the redox reactions in the corresponding active sites. Nevertheless, because of the surface plasmon resonance effects (SPR) of metals such as Ag and Au, the solid-state electron mediators can absorb part of the visible light, thereby affecting the photocatalytic efficiency [22]. In addition, the preparation of ternary systems is complex and the noble metal particles are quite expensive for practical realization. Recently, direct Z-scheme photocatalysts without redox-mediator have also attracted considerable interest. Several direct Z-scheme photocatalysts such as $\text{Ti}_{0.91}\text{O}_2/\text{CdS}$ nanohybrids, $\text{CaIn}_2\text{S}_4/\text{TiO}_2$ and ZnO/CdS composites, have been developed and found to exhibit superior photocatalytic reduction and oxidation activities [23–25].

Low-dimensional nanostructured photocatalysts have attracted increasing attention. For example, one-dimensional (1D) TiO_2 nanobelts as one of the ideal catalysts have been extensively studied owing to their large surface area, high aspect ratio and remarkable morphological features that contribute to transport interfacial charge carriers effectively. Additionally, the high-crystalline TiO_2 nanobelts possess sufficient space for the nucleation and growth of a second phase on its surface to assemble various composite materials [26]. Many heterostructure photocatalysts based on 1D TiO_2 nanobelts showed excellent activity in photocatalytic degradation and water splitting applications [27–30].

Two-dimensional (2D) ZnIn_2S_4 nanosheets are equally interesting because of their layered structures and strong visible absorption

[31–34]. Although studies revealed that ZnIn_2S_4 is activity for hydrogen production under visible light irradiation, the overall photocatalytic efficiency is low due to the short lifetime of the photogenerated electrons resulting from rapid recombination with holes [35,36]. To combine 2D ZnIn_2S_4 nanosheets with 1D TiO_2 nanobelts to form 3D Z-scheme heterostructure may not only increase the surface area, but also improve light absorption. Furthermore, the special 3D interfacial structure may enhance the transfer rate of the photogenerated electrons and holes, leading to a higher photocatalytic activity.

In this work, we have designed and demonstrated a novel 3D Z-scheme photocatalyst nanostructure by assembling ultrathin 2D ZnIn_2S_4 nanosheets onto the surface of 1D TiO_2 nanobelts, as shown in Scheme 1. The obtained 3D Z-scheme $\text{ZnIn}_2\text{S}_4/\text{TiO}_2$ photocatalysts exhibit about 38-times enhancement of photocatalytic activity in the photoreduction of CO_2 compared to bare ZnIn_2S_4 . The hierarchical Z-scheme photocatalysts have great practical applications in photocatalysis.

2. Experimental

2.1. Fabrication of TiO_2 nanobelts

TiO_2 nanobelts were obtained using a previously reported procedure [27]. Typically, P25 (0.4 g) was immersed in NaOH solution (80 mL, 10 M) and stirred for half hour. After sonication for another half hour, the suspension was transferred into a 100 mL Teflon container in a steel keeping at 180°C for 48 h. The resulting gel was filtered, washed repeatedly with deionized water, and then dissolved in HCl (0.1 M) solution for 48 h, and $\text{H}_2\text{Ti}_3\text{O}_7$ nanobelts obtained. The $\text{H}_2\text{Ti}_3\text{O}_7$ nanobelts were then dispersed in a 100 mL Teflon container containing solution of H_2SO_4 (0.02 M) and kept at 100°C for 12 h in an electric oven. Finally, the as-synthesized sample was collected, washed thoroughly with deionized water and finally sintered at 600°C for 2 h, resulting in TiO_2 nanobelts.

2.2. Synthesis of $\text{ZnIn}_2\text{S}_4/\text{TiO}_2$

In a typical experiment, ZnIn_2S_4 nanosheets were synthesized by the modified method reported previously [37], and the $\text{ZnIn}_2\text{S}_4/\text{TiO}_2$ heterostructures at various mole ratios (0.25:1,

0.33:1, 0.50:1 and 1:1) were synthesized. Specifically, ZnCl_2 (0.25–1 mmol), and $\text{InCl}_3 \cdot 4\text{H}_2\text{O}$ (0.5–2 mmol) and thioacetamide (TAA, 1–4 mmol) were dissolved in 20 mL ethylene glycol and stirred half hour at room temperature, to which an appropriate amount (1 mmol) of as-prepared TiO_2 nanobelts was dispersed by sonication for another half hour. The above mixture was maintained in the autoclave with a capacity of 25 mL and heated to 120 °C for 2 h. At last, the products were washed with water and absolute ethanol and dried at 70 °C. Products with different amounts of ZnIn_2S_4 ranging from 0.25 to 1 mmol were denoted as ZIS-0.25/TO, ZIS-0.33/TO, ZIS-0.50/TO and ZIS-1/TO, respectively. For comparison, bare ZnIn_2S_4 nanosheets were also prepared following a similar procedure in the absence of TiO_2 nanobelts.

2.3. Characterizations

X-ray diffraction (XRD) data of the as-synthesized samples were recorded by a Bruker D8A A25X X-ray diffractometer system using $\text{Cu K}\alpha$ ($\lambda = 0.15406 \text{ nm}$) radiation. The morphologies of the prepared samples were performed using a HITACHI S-4800 instrument. High-resolution transmission electron microscopy (HR-TEM) and energy-dispersive X-ray spectroscopy (EDS) were applied to investigate the microstructure using a JEOL JEM-2010 instrument (HR-TEM operated at 200 kV). The UV–vis diffuse reflectance spectra (DRS) of the samples were tested on a TU-1901 double beam spectrophotometer. The photoluminescence (PL) spectra were measured on a high-resolution multi-function imaging spectrometer (FLS 980) and time-resolved photoluminescence (TRPL) measurements were conducted on a Fluorolog-3 Transient State Fluorescence Spectrometer. X-ray photoelectron spectroscopy (XPS) was performed on an K-Alpha spectrometer (THERMO FISHERSCIENTIFIC).

2.4. Photoelectrochemical measurements

Electrochemical and photoelectrochemical (PEC) measurements were conducted using a standard three-electrode quartz cells with Na_2SO_4 electrolyte solution (0.1 M, pH = 6.8). The PEC results were obtained with an electrochemical workstation (CHI-660B, China). A 500 W xenon lamp (Institute for Electric Light Sources, Beijing) was used as the light source for PEC measurements. The Mott-Schottky curves were measured on a fixed frequency of 100 Hz with 5 mV amplitude at various potentials.

2.5. Measurement of photocatalytic CO_2 conversion

Photocatalytic CO_2 reduction was investigated under simulated sun-light. A 300 W Xe lamp was used as light source with the electric current at 10 A. The measurements were performed in a gas-tight system. First, high purity of CO_2 gas was injected into the vacuumed reaction system. Then 0.4 mL of deionized water was added into the reactor. Before light irradiation, CO_2 and H_2O gases were occupied for several hours for the equilibrium of CO_2 and H_2O gases and make sure the adsorption-desorption equilibrium between the photocatalyst (about 0.1 g samples) and gases. The gas products from photocatalytic reactions were periodically monitored and analyzed using gas chromatography (GC-2014, Shimadzu Corp, Japan).

3. Results and discussion

3.1. Structure, morphology and composition of $\text{ZnIn}_2\text{S}_4/\text{TiO}_2$ photocatalyst

The XRD patterns of the as-synthesized $\text{ZnIn}_2\text{S}_4/\text{TiO}_2$ samples with different amounts of ZnIn_2S_4 are shown in Fig. 1. The crys-

tallographic structure of bare ZnIn_2S_4 and TiO_2 are also given for comparison. The X-ray peaks of the TiO_2 powder are in good agreement with anatase phase (JCPDS, No. 21-1272), while the diffraction peaks of ZnIn_2S_4 are identical to that of the hexagonal-phase (JCPDS No. 65-2023) [36,37]. Both TiO_2 and ZnIn_2S_4 phases are observed in the $\text{ZnIn}_2\text{S}_4/\text{TiO}_2$ composites. Moreover, with the increase in ZnIn_2S_4 loadings, the intensity of the diffraction peaks of ZnIn_2S_4 increased, and there is no impurity peaks appearance. These results confirm the co-existence of ZnIn_2S_4 and TiO_2 in the composites materials.

The scanning electron microscopy (SEM) images of TiO_2 with different molar ratios of ZnIn_2S_4 and TiO_2 can be seen in Supplementary Information. Fig. S1a indicates that the surface-coarsened TiO_2 nanobelts with several micrometers in length provide abundant nucleation sites that can be used for assembling another material. The ZnIn_2S_4 synthesized with the hydrothermal self-assemble method consists of monodispersed uniform microspheres with flower-like morphologies (Fig. S1b). After growing with layered ZnIn_2S_4 ultrathin nanosheets, the 3D $\text{ZnIn}_2\text{S}_4/\text{TiO}_2$ structures with fibrous morphology are formed, which is expected to facilitate the transfer of electrons between these two semiconductor materials. The composite photocatalysts with different molar ratios are presented in Fig. S1c–f.

The transmission electron microscope (TEM) images of the final synthesized powder materials are shown in Fig. 2(a–c). It can be seen that the 2D ZnIn_2S_4 nanosheets grow uniformly on the surface-coarsened 1D TiO_2 nanobelts. The HR-TEM images further confirm the close linkage between ZnIn_2S_4 nanosheets and TiO_2 nanobelts. The marked lattice spaces of 0.30 and 0.36 nm are in good agreement with the (102) plane and (101) planes of hexagonal ZnIn_2S_4 and anatase TiO_2 , respectively [38–40]. Besides, the selected area electron diffraction (SAED) image shows two kinds of characteristic spots, which corresponds to the (102) planes of hexagonal-phase ZnIn_2S_4 , and the (101) planes of tetragonal anatase TiO_2 (Fig. 2d). The TEM image in Fig. 2e displays scaly $\text{ZnIn}_2\text{S}_4/\text{TiO}_2$ composite photocatalyst. A large number of ZnIn_2S_4 nanosheets of 100–200 nm in width are well distributed on the surface of TiO_2 nanobelts. The ZnIn_2S_4 nanosheets can improve the visible-light absorption in $\text{ZnIn}_2\text{S}_4/\text{TiO}_2$ composite. Moreover, the 3D structures could shorten the charge transfer time and distance and lead to higher photo-electric conversion efficiency [26]. The $\text{ZnIn}_2\text{S}_4/\text{TiO}_2$ composite structure can be further confirmed in the EDS mappings analysis (see inset of Fig. 2f). The corresponding elemental mappings of Ti are virtually identical with O, which is clear formed the TiO_2 substrates structure. Furthermore, the uniformly distributed elemental mappings of Zn, In, S are similar to each other, and no other elements were detected, which confirms the coexistence of ZnIn_2S_4 and TiO_2 . In addition, the chemical composition of the $\text{ZnIn}_2\text{S}_4/\text{TiO}_2$ composite is supported by energy dispersive spectroscopy (EDS) (see Supplementary Fig. S2). The TEM analysis of TiO_2 nanobelts, ZnIn_2S_4 nanosheets and $\text{ZnIn}_2\text{S}_4/\text{TiO}_2$ composite with different molar ratios are shown in Supplementary Information (Fig. S3).

The X-ray photoelectron spectra (XPS) spectra of TiO_2 , ZnIn_2S_4 and $\text{ZnIn}_2\text{S}_4/\text{TiO}_2$ are shown in Fig. 3. All signals attributable to Ti, O, Zn, In and S are observed for the ZIS-0.33/ TiO_2 nanocomposite. In addition, a weak peak for all samples located at 283.5 eV may be attributed to adventitious carbon derived from the atmospheric CO_2 on the sample surface or from the carbon tape utilized during sample preparation. The survey XPS spectra of other samples with different molar ratios are similar to ZIS-0.33/ TiO_2 (see Supplementary Fig. S4). To thoroughly investigate the interaction between TiO_2 and ZnIn_2S_4 in the $\text{ZnIn}_2\text{S}_4/\text{TiO}_2$ nanocomposites, high resolution XPS spectrum are obtained as shown in Fig. 4. Compared with bare TiO_2 , the binding energy of as-fabricated nanocomposites is neither changed for Ti2p region, nor for O1s (Fig. 4a

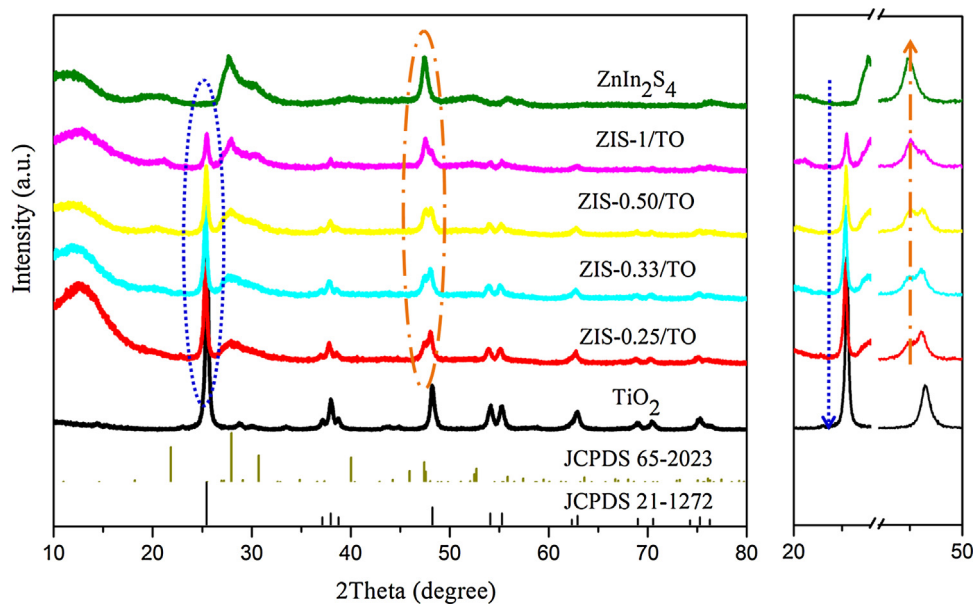


Fig. 1. XRD patterns of the TiO_2 nanobelts, ZnIn_2S_4 nanosheets and $\text{ZnIn}_2\text{S}_4/\text{TiO}_2$ composite materials with different mole ratios.

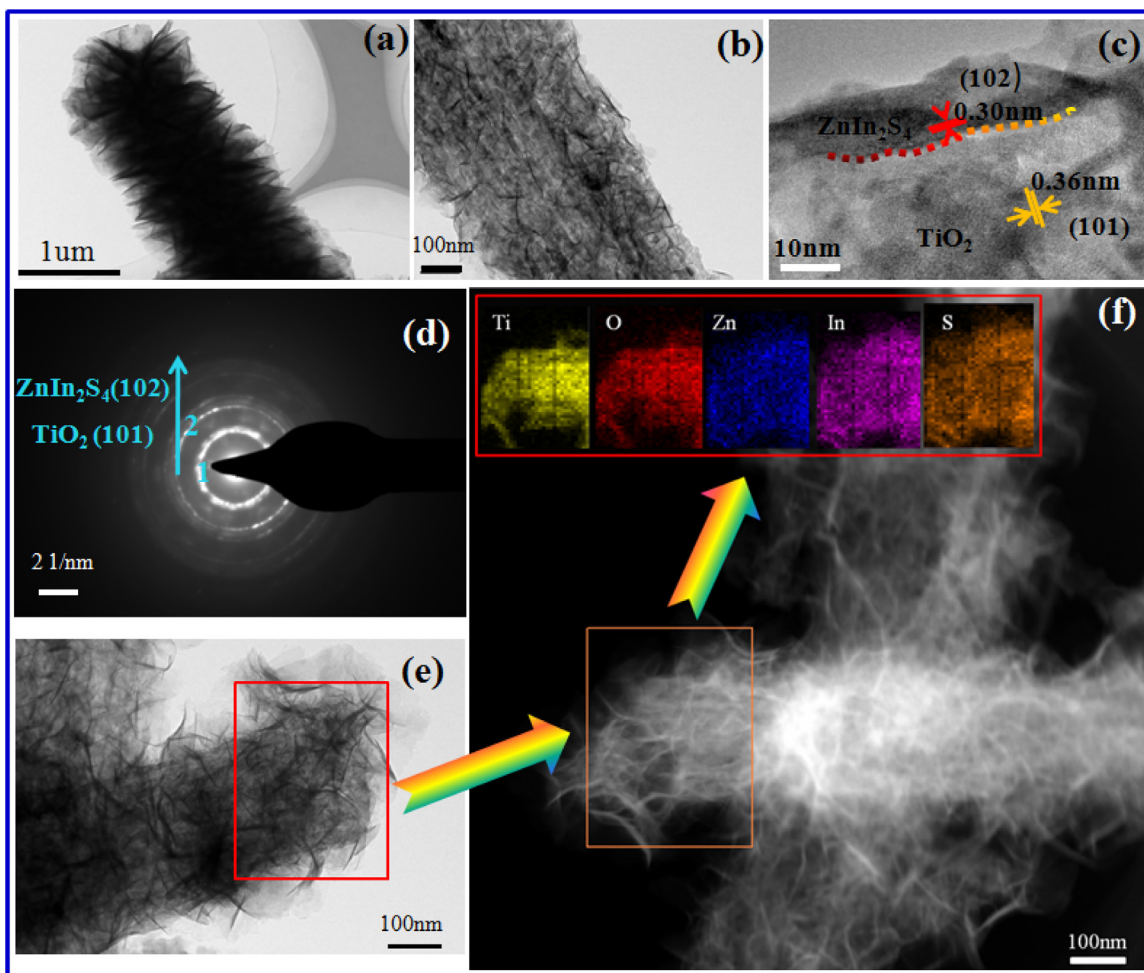


Fig. 2. (a–b) TEM images of ZIS-1/TO ($\text{ZnIn}_2\text{S}_4/\text{TiO}_2$ mol ratio 1:1); (c) HRTEM image of ZIS-0.50/TO ($\text{ZnIn}_2\text{S}_4/\text{TiO}_2$ mol ratio 0.5: 1) and (d) corresponding SAED pattern; (e–f) Selected area for elemental mapping images of Zn, In, S, Ti, and O elements of the ZIS-0.50/TO ($\text{ZnIn}_2\text{S}_4/\text{TiO}_2$ mol ratio 0.5: 1) composite material.

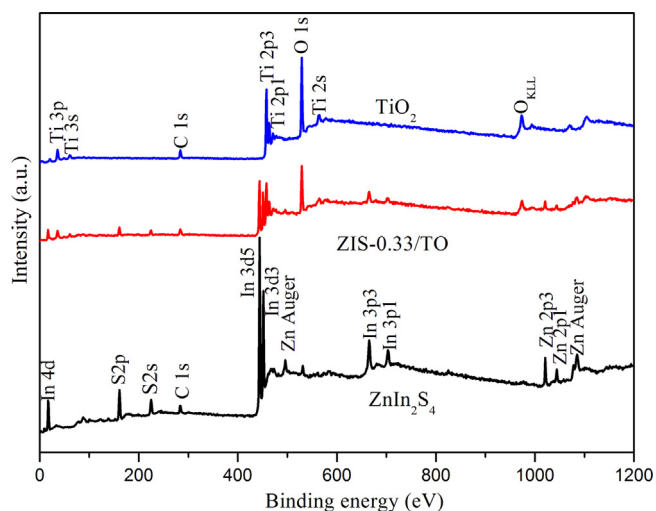


Fig. 3. XPS survey spectra of the as-fabricated TiO_2 , ZnIn_2S_4 and ZIS-0.33/TO ($\text{ZnIn}_2\text{S}_4/\text{TiO}_2$ mol ratio 0.33: 1) nanocomposites.

and b). The characteristic peaks for binding energies located at 1022.5 ($\text{Zn}2\text{p}_{3/2}$), 452.4 ($\text{In}3\text{d}_{3/2}$), 445.2 ($\text{In}3\text{d}_{5/2}$), 161.9 ($\text{S}2\text{p}_{3/2}$) and 162.8 eV ($\text{S}2\text{p}_{1/2}$) can be found from the pristine ZnIn_2S_4 in Fig. 4(c–e), which are fully consistent with values reported in literature [31,41,42] and illustrate the existence of valence states of Zn^{2+} , In^{3+} and S^{2-} , respectively [43]. However, after modification with ZnIn_2S_4 , binding energies of Zn, In and S elements show a slight shift towards lower binding energy, indicating that the binding energies of the core level electrons of these metal and sulfide ions are changed. The results seem to suggest relatively strong interaction between TiO_2 and ZnIn_2S_4 .

UV–vis DRS of TiO_2 , $\text{ZnIn}_2\text{S}_4/\text{TiO}_2$ and ZnIn_2S_4 are given in Fig. S5. The absorption edge of pure TiO_2 nanobelts and ZnIn_2S_4 nanosheets was 380 nm and 467 nm, respectively. According to Tauc formula [$\alpha h\nu = A(h\nu - E_g)^{n/2}$], the band gap of TiO_2 and ZnIn_2S_4 are estimated to 3.26 and 2.65 eV, respectively. Upon the growth of thin ZnIn_2S_4 nanosheets on the surface of TiO_2 nanobelts, a redshift DRS of $\text{ZnIn}_2\text{S}_4/\text{TiO}_2$ composite was observed obvious, and the color of the composite photocatalyst becomes light yellow, which is mainly due to the intrinsic band gap absorption of ZnIn_2S_4 nanosheets [44].

To understand the role between ZnIn_2S_4 nanosheets and TiO_2 nanobelts, the surface area and porosity of bare ZnIn_2S_4 , TiO_2 and $\text{ZnIn}_2\text{S}_4/\text{TiO}_2$ composites have been investigated, as displayed in Fig. S6. The BET surface areas of $\text{ZnIn}_2\text{S}_4/\text{TiO}_2$ composite materials are measured to be $45.6 \text{ m}^2 \text{ g}^{-1}$, higher than that of TiO_2 nanobelts ($39.9 \text{ m}^2 \text{ g}^{-1}$) and ZnIn_2S_4 nanosheets ($23.0 \text{ m}^2 \text{ g}^{-1}$) (see Supplementary Table 1). This kind of porous 3D heterostructure is supposed to be not only beneficial for incident light absorption and photogenerated electron mobility, but also more sites on the surface for adsorption and photoreduction of CO_2 , which improving the photocatalytic CH_4 evolution activities.

3.2. Photocatalytic reduction performances

The photocatalytic measurements for CO_2 reduction into CH_4 were performed under simulated sunlight irradiation. Fig. 5a displays the photocatalytic CH_4 evolution using TiO_2 , ZnIn_2S_4 and $\text{ZnIn}_2\text{S}_4/\text{TiO}_2$ composite with different molar ratios. The pristine TiO_2 nanobelts or ZnIn_2S_4 nanosheets clearly exhibit poor photoreduction activities. For the $\text{ZnIn}_2\text{S}_4/\text{TiO}_2$ composite photocatalyst, there is great improvement of CH_4 generation. After 8 h of UV–vis light irradiation, the CH_4 yield is 1.69, 9.08, 4.01 and $0.90 \mu\text{mol g}^{-1}$ for ZIS-0.25/TO, ZIS-0.33/TO, ZIS-0.50/TO and ZIS-1/TO, respec-

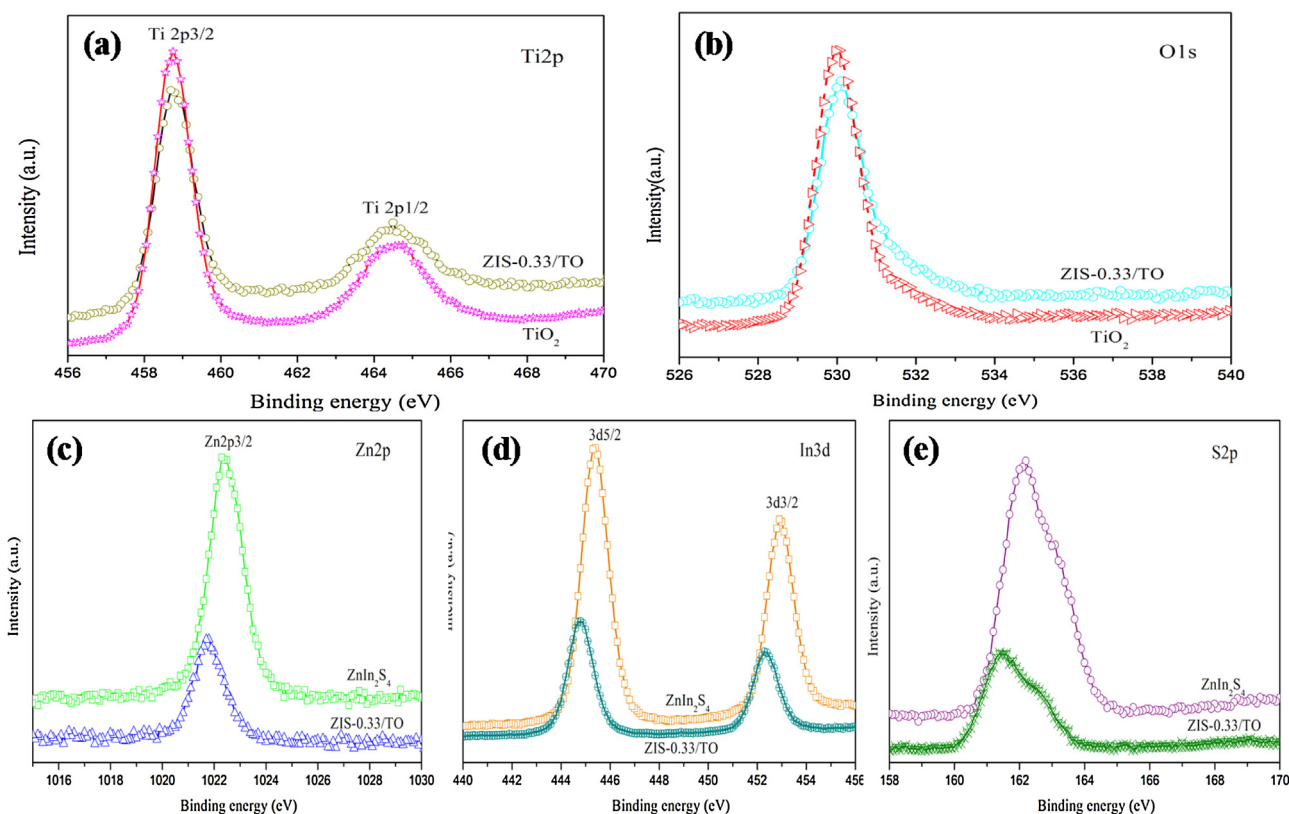


Fig. 4. High resolution XPS spectra of the TiO_2 , ZnIn_2S_4 and ZIS-0.33/TO ($\text{ZnIn}_2\text{S}_4/\text{TiO}_2$ mol ratio 0.33: 1) nanocomposites at different regions: (a) Ti2p, (b) O1s, (c) Zn2p, (d) In3d and (e) S2p.

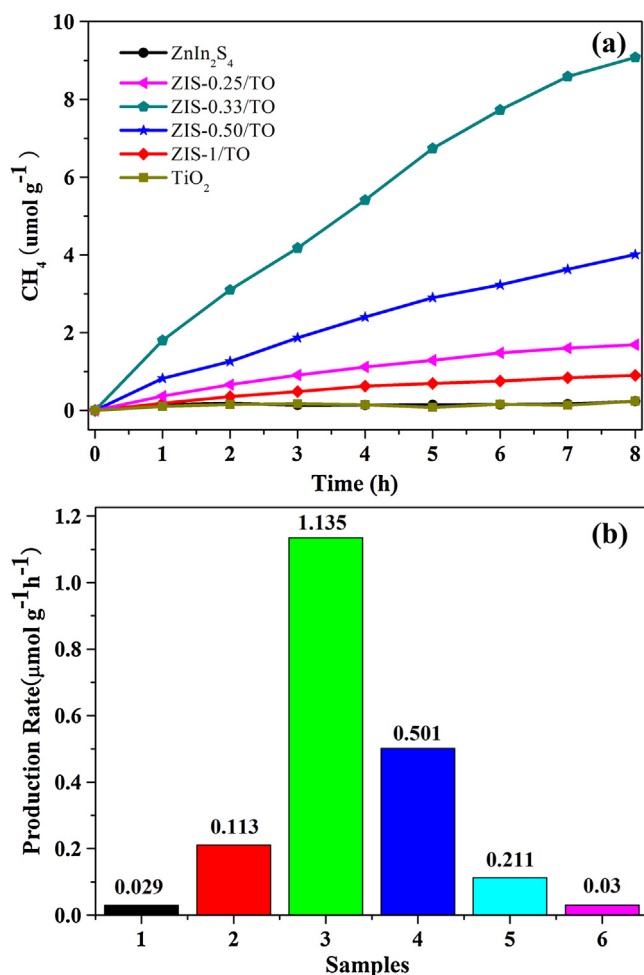


Fig. 5. Evolution activities (a) and CH₄ generation velocity (b) over (1) ZnIn₂S₄ nanosheets; (2) ZIS-0.25/TiO₂ (ZnIn₂S₄/TiO₂ mol ratio 0.25: 1); (3) ZIS-0.33/TiO₂ (ZnIn₂S₄/TiO₂ mol ratio 0.33: 1); (4) ZIS-0.50/TiO₂ (ZnIn₂S₄/TiO₂ mol ratio 0.50: 1); (5) ZIS-1/TiO₂ (ZnIn₂S₄/TiO₂ mol ratio 1: 1); (6) TiO₂ nanobelts.

tively. The corresponding CH₄ production rate of individual ZnIn₂S₄ nanosheets is measured only about 0.029 μmol g⁻¹ h⁻¹. While the CH₄ production rate of ZIS-0.33/TiO₂ (1.135 μmol g⁻¹ h⁻¹) is 39-times higher than that of pristine ZnIn₂S₄ under UV–vis light irradiation (Fig. 5b). The significantly enhanced photocatalytic activity of the ZnIn₂S₄/TiO₂ composite may be the result of improved light and absorption and more effective separation of photoexcited electrons and holes pairs [45–47]. It is also observed that the amount of ZnIn₂S₄ affects the CH₄ evolution activity, partly because the content of ZnIn₂S₄ has great influence on the light absorption as well as charge transfer with TiO₂.

Meanwhile, in the photoreaction proceeded, the CO production is apparent, but the H₂ yield is hardly detected (see Supplementary Fig. S7). Therefore, it could be inferred that the production of CH₄ and CO is from CO₂ photoreduction over ZnIn₂S₄ loaded on TiO₂. However, no oxidative product is detected can be attributed to that O₂ stops at the status of adsorbed •O₂ – (a form of –Ti–O–O–Ti–), which coincides with the previous study [48].

To further understand the mechanism of enhanced of photocatalytic activity of ZnIn₂S₄/TiO₂ composite, the PEC measurements of all samples were performed. As shown in Fig. 6a, the ZIS-0.33/TiO₂ composite photocatalysts exhibit enhanced photocurrents (35 μA/cm²) compared with ZnIn₂S₄ nanosheets (8 μA/cm²) or TiO₂ nanobelts (16 μA/cm²). This is in accordance with the highest photocatalytic reduction of CO₂ into CH₄ under UV–vis light.

This trend is attributed to the intimate interfacial contacts between ZnIn₂S₄ and TiO₂ in the nanocomposites that facilitates interfacial charge transfer and enhances charge separation. In addition, a reasonable current signal is also observed under the visible-light irradiation (Fig. 6b). The above photocurrent results suggest that ZnIn₂S₄ materials can effectively generate photoinduced electrons and without recombining with holes in ZnIn₂S₄/TiO₂ composite material [49].

3.3. Proposed charge transfer mechanism in ZnIn₂S₄/TiO₂ heterostructure

In order to investigate the transfer mechanism of electrons (e⁻) and holes (h⁺) between TiO₂ and ZnIn₂S₄, the bandedge positions of conduction band (CB) and valence band (VB) of the two semiconductor were measured by Mott–Schottky measurement, which can directly probe the energy positions of TiO₂ and ZnIn₂S₄. From Fig. 6c, d, the CB and VB edges of TiO₂ nanobelts are found to be –0.12 eV and +3.14 eV (vs. NHE), and the CB and VB edges of ZnIn₂S₄ nanosheets are –0.65 eV and +2 eV (vs. NHE), respectively. The X-ray photoelectron spectroscopy (XPS) results further confirm band position, which consistent with Mott–Schottky results (see Supplementary Fig. S8 and Table 2). In general, the transfer of the photogenerated electrons or holes between these two semiconductors is regarded as the type-II heterostructure mechanism due to the energy match of TiO₂ and ZnIn₂S₄. Both TiO₂ and ZnIn₂S₄ can be excited and generate the electrons/holes pairs under UV–vis light irradiation. The E_{CB} of ZnIn₂S₄ (–0.65 eV) is more negative than that of TiO₂ (–0.12 eV), thus the excited electrons in ZnIn₂S₄ could directly be injected into the CB of TiO₂ (see Supplementary Fig. S9). Meanwhile, the photogenerated holes in TiO₂ could easily be transferred to the VB of ZnIn₂S₄ since the VB position of ZnIn₂S₄ is much lower than that of TiO₂. However, for CO₂ and H₂O photoreduction reaction, the lowest reduction potential required for CO₂ to be converted into CH₄ is E° = –0.24 eV vs normal hydrogen electrode (NHE) (CO₂ + 8e⁻ + 8H⁺ → CH₄ + 2H₂O) [21]. If the photogenerated electrons in ZnIn₂S₄ are injected into the CB of TiO₂, the accumulated electrons in the CB of TiO₂ could not reduce CO₂ into CH₄ because the CB position of TiO₂ has a reduction potential (–0.12 eV) lower than that required for the reduction of CO₂. Hence, we infer that it is impossible for the ZnIn₂S₄/TiO₂ type-II heterostructure photocatalyst to induce direct reduction of CO₂ into CH₄.

The charge transfer mechanism of the present ZnIn₂S₄/TiO₂ composite for the CO₂ photoreduction can be proposed based on a direct Z-scheme photocatalytic system, as shown in Fig. 7. When the ZnIn₂S₄/TiO₂ heterojunction is irradiated by light, the electrons in TiO₂ with a relatively low CB edge may recombine with the holes in ZnIn₂S₄ nanosheets that have a relatively high VB at the solid heterostructure interface. Consequently, more reductive electrons and oxidative holes would accumulate in the CB of ZnIn₂S₄ and VB of TiO₂, thereby resulting in enhanced photocatalytic activity for reduction of CO₂. To further elucidate the formation and transfer/transport dynamics of photoinduced charge carriers in the Z-scheme ZnIn₂S₄/TiO₂ system, we carried out photoluminescence (PL) and time-resolved photoluminescence (TRPL) measurements on the samples excited at 266 nm by laser. As observed in Fig. S10, the PL decay traces of ZnIn₂S₄ and TiO₂ show short PL lifetime of 0.275 and 0.43 ns, respectively. However, the ZnIn₂S₄/TiO₂ composite sample shows much longer PL decay lifetime, 1.212 ns. The prolonged decay lifetime suggests that the electron-hole recombination could be effectively prohibited for ZnIn₂S₄/TiO₂, so the quantum efficiency of the samples is improved [47]. Further research as shown in Fig. S11a, it could be clearly seen that the TiO₂ nanobelts show a wide peak at 470 nm, which possibly demonstrates that the excitonic PL mainly results from surface oxygen vacancies and defects, and several excitonic

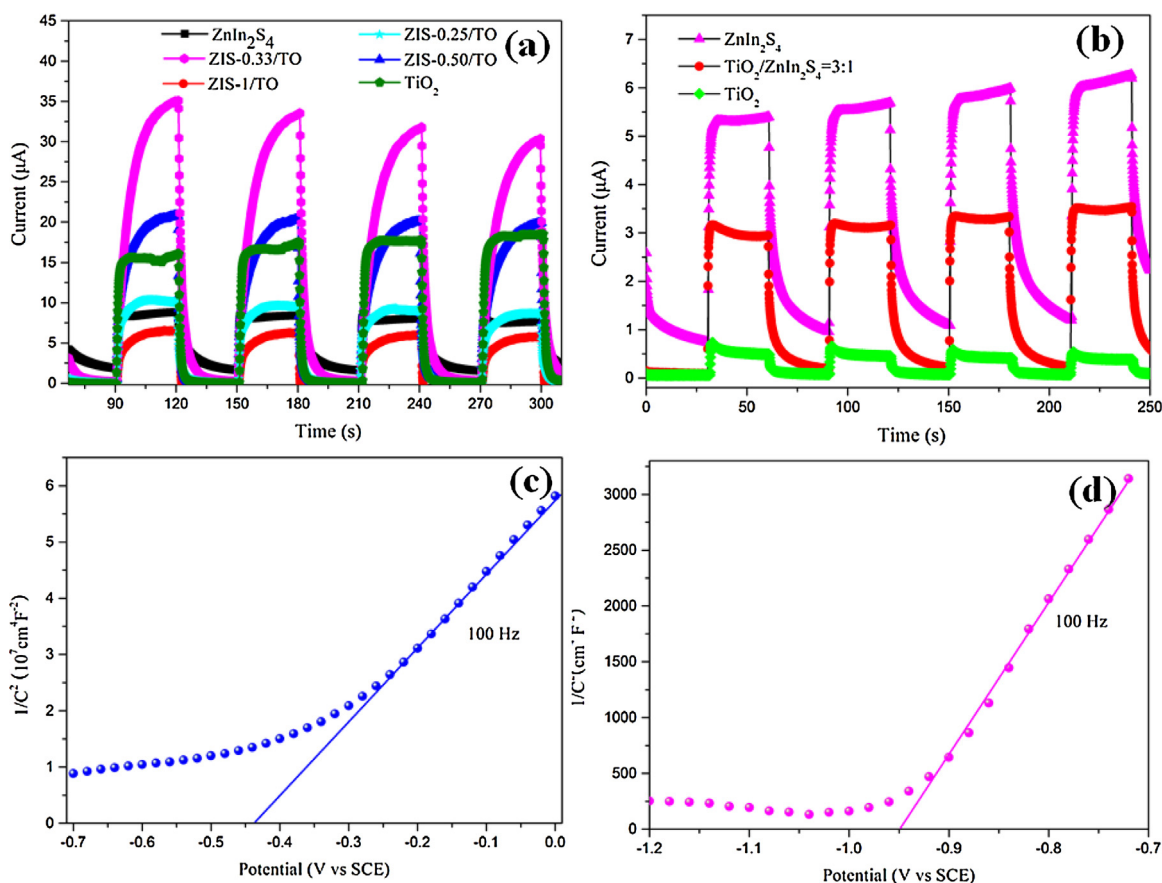


Fig. 6. (a) Photogenerated currents density of ZnIn₂S₄ nanosheets, ZnIn₂S₄/TiO₂ composite and TiO₂ nanobelts samples under UV–vis light; (b) Photogenerated currents density of ZnIn₂S₄ nanosheets ZnIn₂S₄/TiO₂ (mole ratio 0.33:1) and TiO₂ nanobelts products under visible light; (c) Mott-Schottky plot for TiO₂ nanobelts and (d) ZnIn₂S₄ nanosheets electrode in saturated Na₂SO₄ electrolyte solution (0.1 M, pH = 6.8) vs SCE.

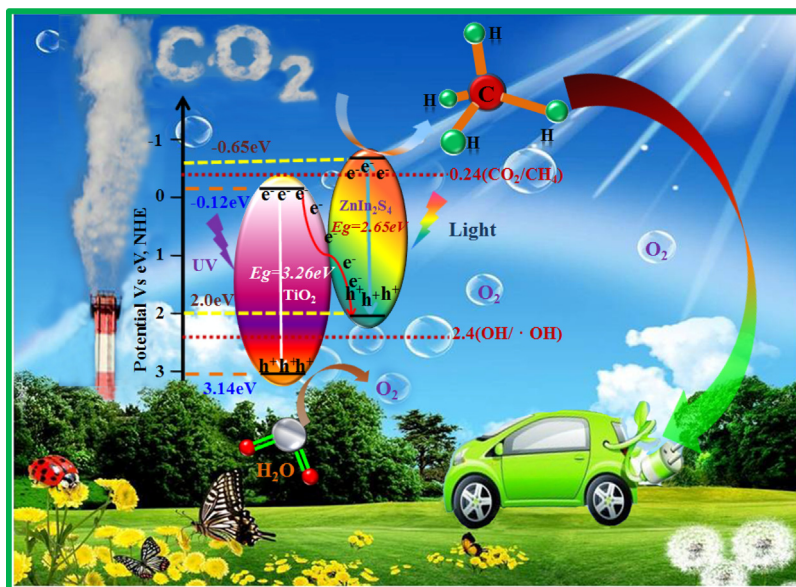


Fig. 7. Schematic diagrams for energy bands of TiO₂ nanobelt and ZnIn₂S₄ nanosheet and the transfer of photogenerated electrons from TiO₂ to ZnIn₂S₄ forming Z-scheme system under UV–vis light irradiation.

PL peaks can illustrate that the surface states or defects are abundant [50]. The ZnIn₂S₄ nanosheets also exhibit four strong emission peaks at 470 nm, 560 nm, 650 nm and 680 nm, respectively. The PL peak at 470 nm is attributed to band edge free exciton, and that at 560 nm, 650 nm and 680 nm might due to the excitonic PL process

resulting from defects [51,52]. Moreover, it is very interesting that the shape of PL spectra of ZnIn₂S₄/TiO₂ heterostructures is different from both TiO₂ nanobelts and ZnIn₂S₄ nanosheets on the same condition. The band edge free exciton peak of ZnIn₂S₄ unchanged but the defects peaks disappeared. Besides, a new peak at 580 nm

is appeared, which may be the outcome of combing with TiO₂ nanobelts. More detailed information excited by 500 nm shown in Fig. S11b, it can be seen that the emission peak of ZnIn₂S₄/TiO₂ are shifted to 581 nm, which is almost equal to the band gap energy between VB of ZnIn₂S₄ and the CB of TiO₂ nanosheets (2.12 eV). These results are consistent with the proposal that electrons in the CB of TiO₂ nanosheets recombine with the holes in the VB of ZnIn₂S₄ in a Z scheme system [23].

4. Conclusion

In summary, a solar light-driven 3D Z-scheme photocatalyst by assembling ultrathin 2D ZnIn₂S₄ nanosheets onto 1D TiO₂ nanobelts has been successfully demonstrated for photocatalytic reduction of CO₂ into CH₄. This artificial Z-scheme system shows a CH₄ production rate up to 1.135 $\mu\text{mol g}^{-1} \text{h}^{-1}$, which is about 39-times higher than that of bare ZnIn₂S₄ (0.029 $\mu\text{mol g}^{-1} \text{h}^{-1}$) nanosheets. This special 3D interfacial structure was shown to effectively promote the recombination of the photogenerated electrons of TiO₂ nanobelt with the holes of ZnIn₂S₄ nanosheets, resulting in an enrichment of photogenerated electrons in the conduction band of ZnIn₂S₄ and consequently higher photocatalytic reduction property. This study also provides new insight into the design and underlying mechanism of direct Z-scheme for enhanced photocatalysis.

Acknowledgements

This work is supported by the National Natural Science Foundations of China (Grant No. 21577132), the Fundamental Research Funds for the Central Universities (Grant No. 2652015225).

Appendix A. Supplementary data

Supplementary data associated with this article can be found, in the online version, at [10.1016/j.apcatb.2017.08.016](https://doi.org/10.1016/j.apcatb.2017.08.016).

References

- [1] Q. Liu, D. Wu, Y. Zhou, H. Su, R. Wang, C. Zhang, S. Yan, M. Xiao, Z. Zou, *ACS Appl. Mater. Interfaces* 6 (2014) 2356–2361.
- [2] Y. Zhou, Z. Tian, Z. Zhao, Q. Liu, J. Kou, X. Chen, J. Gao, S. Yan, Z. Zou, *ACS Appl. Mater. Interfaces* 3 (2011) 3594–3601.
- [3] S.N. Habisreutinger, L. Schmidt-Mende, J.K. Stolarczyk, *Angew. Chem. Int. Ed.* 52 (2013) 7372–7408.
- [4] E.V. Kondratenko, G. Mul, J. Baltrusaitis, G.O. Larrazabal, J. Perez-Ramirez, *Energy Environ. Sci.* 6 (2013) 3112–3135.
- [5] P. Li, H. Xu, L. Liu, T. Kako, N. Umezawa, H. Abe, J. Ye, *J. Mater. Chem. A* 2 (2014) 5606–5609.
- [6] K. Li, X. An, K.H. Park, M. Khraisheh, J. Tang, *Catal. Today* 224 (2014) 3–12.
- [7] H.J. Li, Y. Zhou, W.G. Tu, J.H. Ye, Z.G. Zou, *Adv. Funct. Mater.* 25 (2015) 998–1013.
- [8] P. Zhou, J.G. Yu, M. Jaroniec, *Adv. Mater.* 26 (2014) 4920–4935.
- [9] Y. Tachibana, L. Vayssieres, J.R. Durrant, *Nat. Photonics* 6 (2012) 511–518.
- [10] H. Tada, T. Mitsui, T. Kiyonaga, T. Akita, K. Tanaka, *Nat. Mater.* 5 (2006) 782–786.
- [11] A. Iwase, Y.H. Ng, Y. Ishiguro, A. Kudo, R. Amal, *J. Am. Chem. Soc.* 133 (2011) 11054–11057.
- [12] K. Sekizawa, K. Maeda, K. Domen, K. Koike, O. Ishitani, *J. Am. Chem. Soc.* 135 (2013) 4596–4599.
- [13] P. Li, Y. Zhou, H. Li, Q. Xu, X. Meng, X. Wang, M. Xiao, Z. Zou, *Chem. Commun.* 51 (2015) 800–803.
- [14] K. Maeda, *ACS Catal.* 3 (2013) 1486–1503.
- [15] Y. Qu, X. Duan, *Chem. Soc. Rev.* 42 (2013) 2568–2580.
- [16] H. Kato, Y. Sasaki, N. Shirakura, A. Kudo, *J. Mater. Chem. A* 1 (2013) 12327–12333.
- [17] P.J. Yang, J.H. Zhao, J. Wang, B.Y. Cao, L. Li, Z.P. Zhu, *J. Mater. Chem. A* 3 (2015) 8256–8259.
- [18] Y. Sasaki, H. Nemoto, K. Saito, A. Kudo, *J. Phys. Chem. C* 113 (2009) 17536–17542.
- [19] Z. Wang, B. Huang, Y. Dai, Y. Liu, X. Zhang, X. Qin, J. Wang, Z. Zheng, H. Cheng, *CrystEngComm* 14 (2012) 1687–1692.
- [20] H.J. Li, Y.Y. Gao, Y. Zhou, F.T. Fan, Q.T. Han, Q.F. Xu, X.Y. Wang, M. Xiao, C. Li, Z.G. Zou, *Nano Lett.* 16 (2016) 5547.
- [21] A. Iwase, Y.H. Ng, Y. Ishiguro, A. Kudo, R. Amal, *J. Am. Chem. Soc.* 133 (2011) 11054.
- [22] H.J. Li, W.G. Tu, Y. Zhou, Z.G. Zou, *Adv. Sci.* 3 (2016) 1500389.
- [23] W.G. Tu, Y. Zhou, S.H. Feng, Q.F. Xu, P. Li, X.Y. Wang, M. Xiao, Z.G. Zou, *Chem. Commun.* 51 (2015) 13354–13357.
- [24] W.K. Jo, T.S. Natarajan, *ACS Appl. Mater. Interfaces* 7 (2015) 17138–17154.
- [25] X.W. Wang, G. Liu, Z.G. Chen, F. Li, L.Z. Wang, G.Q. Lu, H.M. Cheng, *Chem. Commun.* 345 (2009) 2–3454.
- [26] J. Tian, Z.H. Zhao, A. Kumar, R.I. Boughton, H. Liu, *Chem. Soc. Rev.* 43 (2014) 6920–6937.
- [27] J. Tian, Y. Sang, Z. Zhao, W. Zhou, D. Wang, X. Kang, H. Liu, J. Wang, S. Chen, H. Cai, *Small* 9 (2013) 3864–3872.
- [28] G.H. Chen, S.Z. Ji, Y.H. Sang, S.J. Chang, Y.N. Wang, P. Hao, J. Claverie, H. Liu, *Nanoscale* 7 (2015) 3117–3125.
- [29] J. Tian, P. Hao, N. Wei, H.Z. Cui, H. Liu, *ACS Catal.* 5 (2015) 4530–4536.
- [30] Z.X. Chen, D.Z. Li, W.J. Zhang, Y. Shao, T.W. Chen, M. Sun, X.Z. Fu, *J. Phys. Chem. C* 11 (2009) 4433–4440.
- [31] W. Chen, T.Y. Liu, T. Huang, X.H. Liu, X.J. Yang, *Nanoscale* 8 (2016) 3711–3719.
- [32] X.L. Gou, F.Y. Cheng, Y.H. Shi, L. Zhang, S.J. Peng, J. Chen, P.W. Shen, *J. Am. Chem. Soc.* 128 (2006) 7222–7229.
- [33] Z.B. Lei, W.S. You, M.Y. Liu, G.H. Zhou, T. Takata, M. Hara, K. Domen, C. Li, *Chem. Commun.* (2003) 2142–2143.
- [34] L. Shang, C. Zhou, T. Bian, H.J. Yu, L.Z. Wu, C.H. Tung, T.R. Zhang, *J. Mater. Chem. A* 1 (2013) 4552–4558.
- [35] B. Gao, L.F. Liu, J.D. Liu, F.L. Yang, *Appl. Catal. B-Environ.* 129 (2013) 89–97.
- [36] Y.H. Gao, H.X. Lin, S.Y. Zhang, Z.H. Li, *RSC Adv.* 6 (2016) 6072–6076.
- [37] Y.J. Chen, S.W. Hu, W.J. Liu, X.Y. Chen, L. Wu, X.X. Wang, P. Liu, Z.H. Li, *Dalton Trans.* 40 (2011) 2607–2613.
- [38] G. Yang, H. Ding, D.M. Chen, W.H. Ao, J. Wang, X.F. Hou, *Appl. Surf. Sci.* 376 (2016) 227–235.
- [39] S.H. Shen, L. Zhao, L.J. Guo, *J. Phys. Chem. Solids* 69 (2008) 2426–2432.
- [40] J.X. Zhang, B.S. Li, W.L. Yang, *Mater. Lett.* 117 (2014) 252–255.
- [41] J.G. Hou, C. Yang, H.J. Cheng, Z. Wang, S.Q. Jiao, H.M. Zhu, *Phys. Chem. Chem. Phys.* 15 (2013) 15660–15668.
- [42] G.H. Tian, Y.J. Chen, Z.Y. Ren, C.G. Tian, K. Pan, W. Zhou, J.Q. Wang, H.G. Fu, *J. Chem. Asian* 9 (2014) 1291–1297.
- [43] H. Liu, Z.T. Jin, Z.Z. Xu, Z. Zhang, D. Ao, *RSC Adv.* 5 (2015) 97951–97961.
- [44] J. Zhou, G. Tian, Y. Chen, X. Meng, Y. Shi, X. Cao, K. Pan, H. Fu, *Chem. Commun.* 49 (2013) 237–239.
- [45] Q. Gu, J. Long, Y. Zhou, R. Yuan, H. Lin, X. Wang, *J. Catal.* 289 (2012) 88–99.
- [46] J. Long, W. Xue, X. Xie, Q. Gu, Y. Zhou, Y. Chi, W. Chen, Z. Ding, X. Wang, *Catal. Commun.* 16 (2011) 215–219.
- [47] H. Zhuang, Q. Gu, J. Long, H. Lin, H. Lin, X. Wang, *RSC Adv.* 4 (2014) 34315–34324.
- [48] D.W. Li, S.X. Ouyang, H. Xu, D. Lu, M. Zhao, X.L. Zhang, J.H. Ye, *Chem. Commun.* 52 (2016) 5989–5992.
- [49] Y. Du, D.M. Chen, Z.H. Wang, H. Ding, R.L. Zong, Y.F. Zhu, *Phys. Chem. Chem. Phys.* 16 (2014) 26314–26321.
- [50] L.Q. Jing, B.F. Xin, D.J. Wang, F.L. Yuan, H.G. Fu, J.Z. Sun, *Chem. J. Chin. Univ.* 26 (2005) 111–117.
- [51] K.L. Song, R.S. Zhu, F. Tian, G. Cao, J. Feng Ouyang, *Solid State Chem.* 232 (2015) 138–143.
- [52] L.Q. Jing, Y.C. Qu, B.Q. Wang, S.D. Li, B.J. Jiang, L.B. Yang, W. Fu, H.G. Fu, J.Z. Sun, *Sol. Energy Mater. Sol. C* 90 (2006) 1773–1787.